Title: Intracellular tension relaxation engineered through D-enantiomeric hydrogel maneuvers neurogenesis and immunomodulation to facilitate spinal cord repair

Authors: Ya Li[1, 2]†, Yulin Wang[1]†, Xinyu Fang[1], Hengtong Zhang[1], Ruicheng Li[1], Rupeng Cai[1], Xiaohui Li[1], Zhaopu Yang[1], Xiaoyun Li[1], Zhongbing Huang[1], Guangfu Yin[1], Qiang Ao[1, 2, 3]*

Affiliations:

[1]College of Biomedical Engineering, Sichuan University; Chengdu, 610065, China.

[2]Institute of Regulatory Science for Medical Devices, Sichuan University; Chengdu, 610065, China.

[3]NMPA Key Laboratory for Quality Research and Control of Tissue Regenerative Biomaterial & National Engineering Research Center for Biomaterials, Sichuan University; Chengdu, 610065, China

*Corresponding author. Email: aoqiang@scu.edu.cn

Abstract: Microenvironment mechanics plays a vital role in regulating morphogenesis and immune response after injury, but their exploration has been hindered by the fragile mechanical strength and oxidative physiological environment in spinal cord injury (SCI). Here, we engineered self-assembly hydrogels of enantiomeric peptides with neural tissue-matching mechanical properties to persistently manipulate cellular membrane tension and mechanotransduction through stereo conformational recognition and consequent protein affinity difference. The D-enantiomeric hydrogel-induced intracellular tension relaxation activates neurogenesis and ECM remolding in astrocytes, suppresses pro-inflammation and promotes pro-regeneration in microglia, which significantly facilitates neuroprotection and functional recovery in a rat severe SCI model. The intracellular tension relaxation-induced morphogenesis may be neural characteristics, contrary to non-neural cells, as the downstream mechanical signaling is activated by the resulted neurogenic morphology change. Overall, inducing intracellular tension relaxation is a potential effective strategy for promoting nerve regeneration.

Main Text: The absent neurogenesis and inflammation-driven secondary damage present two primary challenges in spinal cord injury (SCI) (*1, 2*), resulting from highly specialized neural cytoskeleton precisely structured for efficient information transmission in the nerve system (*3*). Over recent decades, efforts have focused on biochemical interventions, such as growth factor cocktail (*4*), stem cells (*5, 6*) and diverse bioactive components (*7, 8*), to regulate responsive neural cells and inflammation. Yet, the role of mechanical cues from extracellular matrix (ECM), where cells reside and are shaped, has often been underemphasized. Mechanical signals from microenvironment regulate cell fate and shape morphogenesis (*9, 10*), both of which are crucial for neurogenesis (*11, 12*) and immunomodulation (*13, 14*), whereas mechanical properties alter dramatically after SCI as cysts, cavities, and glial scar form in the lesion (*15, 16*). Nonetheless, our understanding of how mechanics impact neural cells and immune responses post-SCI remains poorly understood. One major challenge is that traditional methods for engineering ECM mechanics, such as adjusting crosslinking density or adhesion ligand concentration (*17, 18*), struggle to maintain a persistent mechanical gradient in the oxidative, enzyme-rich physiological environment, particularly within the weak strength range of central neural tissue from 100 to 1000 Pa (*19*).

Cells detect microenvironment mechanics through conformational recognition between adhesion ligands and membrane receptors (*20*). Consequently, engineered enantiomeric ECM, as a stereoisomerism that discriminates protein affinity (*21*), enables refined and stable mechanosensing gradients while maintaining identical chemical and mechanical environments (*22*), providing an alternative approach to exploring ECM mechanobiology. Compared to reported proliferation and differentiation improvement by L-enantiomeric ECM with stronger adhesion binding across multiple non-neural cell models (*23-27*), our previous work reveals that D-enantiomeric ECM notably promotes several morphogenetic processes in neurons and glial cells (*28, 29*), consistent with other reports on neural activity and differentiation enhancement (*30-32*). This exclusive enantiomer-reverse mechanical response in neural cells implies that neurogenesis may require idiosyncratic mechanical properties for regeneration. Meanwhile, immune responses to ECM mechanics have also shown enantiomer-specific effects, with distinct levels of inflammation and even opposite regulatory effects (*33-36*). However, studies utilizing different enantiomers with different immune cell models have yet to establish consistent patterns. In central nervous system, microglia are specialized resident immune cells crucial in secondary inflammatory damage following SCI (*1, 37*). Elucidating the immune effects of microglia responding to mechanical cues using enantiomeric ECM is also critical for clarifying the ECM mechanobiology necessary for SCI restoration.

Here, we engineered enantiomeric hydrogels with neural tissue-matching mechanical properties to manipulate cellular tension and mechanotransduction through different protein affinity. D-enantiomeric hydrogel-induced intracellular tension relaxation activates neurogenesis and ECM remolding in astrocytes, suppresses pro-inflammation and promotes pro-regeneration in microglia. In a severe SCI rat model, D-gel treatment significantly mitigates inflammatory damage and facilitates functional recovery. Single nucleus RNA sequence reveals that the neurogenesis and immunomodulation protect neuron from degeneration and enhances synaptic reconstruction and neuronal communication. We also find out that the intracellular tension relaxation-induced morphogenesis may be characteristic in neural cells as the mechanical signaling is activated by the consequent neurogenic morphology change.

Enantiomeric hydrogel preparation and characterization

To establish symmetrical chirality, we synthesized bioactive ligand-excluded tripeptide enantiomers, N-(9-fluorenylmethoxycarbonyl)-protected phenylalanine-phenylalanine-aspartic

acid (Fmoc-^{D}F^{D}F^{D}D and Fmoc-^{L}F^{L}F^{L}D, fig. S1), to self-assembly into supramolecular hydrogels (D-gel and L-gel, Fig. 1A, fig. S2A and B). The polarized light absorption signals of equal intensity but opposite signs from circular dichroism (CD) spectra (Fig. 1B) validated the mirror-symmetrical chirality between enantiomeric molecules and supramolecular structures. The D-gel and L-gel have identical mechanical strength (G' ~800 Pa, G" ~130 Pa, Fig. 1C), and stress relaxation profile (Fig. 1D), matching central nervous tissues *(19)*. And their rheological strength exhibited improvement in response to cerebrospinal fluid under oscillatory shear load (fig. S2C), facilitating self-healing and injectability. Electron microscopy observations (Fig. 1E, fig. S2D and E) revealed the helical nanofibers in hydrogels with equivalent diameters and helical pitches (fig. S2F and G) but opposite helical directions. Furthermore, small-angle X-ray scattering (SAXS, Fig. 1F) confirmed analogous filament formation, exhibiting nearly identical Guinier region slopes (-1.46 and -1.47). The peak at 0.019 $Å^{-1}$ (d-spacing 330 Å) suggested supramolecular hierarchical stacking and periodic arrangement, consistent with the helical structure. The identical peaks of enantiomeric wide-angle X-ray scattering (WAXS, Fig. 1G) at 1.9 $Å^{-1}$ (d-spacing ~3.3 Å) and 2.25 $Å^{-1}$ (d-spacing ~2.8 Å) corresponded to relaxed lateral stacking of β-strands and compactly ordered sequential stacking, respectively. The molecular dynamic (MD, fig. S2H) simulation confirmed that the enantiomers assembly through π-π stacking of hydrophobic aromatic groups in the filament interior, while a few hydrogen bonds form between the hydrophilic ends of aspartic acid on the exterior. Collectively, we developed mirror-symmetrical enantiomeric hydrogels with identical non-stereochemical properties, central nervous tissue-equivalent mechanical properties, and cerebrospinal fluid-responsive self-healing.

Enantiomer-dependent cellular adhesion mechanics

Since adhesion ligands were excluded in the FFD sequence, assembly-attracted proteins solely provide ECM anchors for mechanosensing *(38)*. We simulated the MD of physical interactions between enantiomeric assemblies and fibronectin/laminin, both of which possess integrin binding ligands *(39, 40)*, revealing that hydrogen bonds were predominant (fig. S3) and formed fewer between D-assembly and both proteins (Fig. 1H). Interaction energy analyses corroborated that electrostatic energy (E_{Coul}), contributing to hydrogen bonds *(41)*, dominated in the interactions, with Van der Waals energy (E_{VdW}) nearly negligible (Fig. 1I). The negative sign and lower absolute E_{Coul} values validated the weaker attraction between D-assembly and both adhesive proteins. These simulations verify that D-gel possesses weaker protein affinity compared to L-gel, potentially facilitating detachment during cell adhesion.

We then quantified the adhesion force between cells and enantiomeric hydrogels using a single-cell force spectroscopy (SCFS). Standard cell culture plates treated for high adhesion were used as control. The adhesion force on D-gel was significantly reduced, reaching 0.48-fold of the L-gel group and 0.45-fold of the control group (Fig. 1J). The adhesion force distribution also differed (Fig. 1K), with the D-gel group exhibited a single sharp peak corresponding to the central cell body, whereas the L-gel and control groups displayed an additional flatter peak attributing to the long protrusion characteristic of neural cells (Fig. 1L). These results substantiate that the cellular mechanosensing on engineered hydrogels is enantiomer-dependent. Adhesive anchors on D-gel are diminished and confined to the cell body, whereas on the L-gel group, adhesion is stronger and extends to the cell protrusions, resembling high-adhesion culture.

Chirality mechanics-driven FA distribution and intracellular tension

Adhesion force is generated via focal adhesion (FA) *(42)*, within which transmembrane integrins sense and clutch ECM binding sites *(43)*, The immunofluorescence (IF) images (Fig. 1M) revealed a diffuse integrin β1 distribution in astrocytes with a spread cytoskeletal morphology

and retracted protrusions on D-gel, compared to its conspicuously clustering at both the cell body and slender protrusions in the L-gel and control groups. Talin, linking integrin and cytoskeleton, also exhibited diffuse distribution on D-gel and clustered orientation along protrusions on L-gel and high-adhesion surface (Fig. 1N). The lack of integrin and talin clustering on D-gel indicates the immaturity of FAs, resulting in unstable mechanical anchoring *(43)*. Paxillin (Fig. 1O), FA scaffold protein that facilitates FA stabilization and indicates cytoskeleton movement *(44)*, formed clusters distributed along cytoskeleton edge without orientation on D-gel, whereas aligned along the protrusions in the L-gel and control groups. Vinculin (Fig. 1P), cytoskeleton linkers in FAs *(45)*, exhibited perinuclear loose clustering on D-gel, whereas extended to the anterior protrusion with highly clustering in the L-gel and control groups. These results suggest that in astrocytes cultured on D-gel, immature and fragile FAs form, which are prone to rapid disassembly, providing unstable anchorage and disrupting cytoskeletal alignment. In contrast, mature, stable FA clusters form in the bipolar or tripolar morphology and neurogenic cellular protrusions of astrocytes cultured on L-gel and high-adhesion control surfaces. Additionally, this FA distribution pattern and cellular morphology on D-gel conforms to the SCFS characteristics of weaker adhesion force and absence of a secondary protrusion force peak (Fig. 1J to L).

The mechanical force sensed by FAs is subsequently transmitted to cytoskeleton *(46)*. The lowest level of p-myosin IIa (force generator in cytoskeleton *(47)*) on D-gel (Fig. 1Q and R) indicated cytoskeleton tension diminution. We then measured cytoskeleton force directly using Förster resonance energy transfer (FRET) technology *(48)*, where force-induced separation of the two fluorophores reduces the energy transfer efficiency (Fig. 1S). The increased FRET efficiency on D-gel (Fig. 1T, fig. S4, 1.21-fold of the L-gel group and 1.11-fold of the control group) validated the significant intracellular tension relaxation. In summary (as illustrated in Fig. 1U), insufficient protein affinity detaches integrin-binding proteins from D-gel (Fig. 1H and I, S3) under mechanical adhesion force (Fig. 1J to L), impairing FA maturation and stabilization (Fig. 1M to P) and resulting in intracellular tension relaxation (Fig. 1Q to T, fig. S4), compared to high-adhesion L-gel. Although derived from astrocytes, this theory is based on enantiomer-dependent protein affinity and can be extended to other cell types. We successfully engineered enantiomeric hydrogel-driven mechanosensing and mechanotransduction manipulation.

Intracellular tension relaxation facilitates morphogenesis in neural cells

Subsequently, we assessed the impacts of manipulated mechanotransduction on morphogenesis processes in astrocytes. Consistent with our previous findings *(29)*, astrocytes cultured on D-gel with low intracellular tension exhibited significantly enhanced viability (Fig. 2A, fig. S5A), proliferation (Fig. 2B and C, fig. S5B and C), and survival (anti-apoptosis, Fig. 2D, fig. S5D), compared to the L-gel group with high tension. Moreover, the increased mitochondrial membrane potential (MMP, Fig. 2E, fig. S5E) and elevated adenosine triphosphate (ATP) level (Fig. 2F) indicated that intracellular tension relaxation protected mitochondria from depolarization and facilitated energy metabolism in astrocytes. Cellular migration was also accelerated (fig. S5F) with a rate of ~31% after 24 h, 1.7-fold of L-gel group (Fig. 2G). Intracellular tension relaxation comprehensively promoted fundamental morphogenesis processes.

To gain a deeper insight, we analyzed global gene expression profile of astrocytes under manipulated intracellular tension (high-adhesion culture plate was again used as high-tension control here, fig. S6A and B). The transcriptome on D-gel underwent substantial changes compared to the similar L-gel and control groups (fig. S6C). The upregulated genes were annotated (fig. S6D) and analyzed through gene ontology (GO) enrichment (Fig. 2H), revealing their predominant involvement in cell-ECM interactions (9 of the top 20 terms) and

morphogenesis (10 of the top 20 terms). Further hierarchical clustering of cell-ECM interaction-related genes (Fig. 2I) showed that D-gel upregulated genes encoding ECM components and ECM proteases, while downregulating protease inhibitors. Meanwhile, hierarchical clustering of morphogenesis-related genes (Fig. 2J) revealed that D-gel upregulated genes encoding growth factors, neurogenesis-positive regulators and transcription factors, while downregulating neurogenesis inhibitors. These results highlight that intracellular tension relaxation initiates a dynamic process of extracellular matrix construction and remodeling, while promoting neurogenesis activation, which is essential for nerve regeneration.

Intracellular tension relaxation induces pro-regenerative responses in microglia

Regarding immune response, most genesis processes of microglia showed no significant nor coherent difference under different tensions (fig. S7A to E). However, the apoptosis on D-gel is decreased (fig. S7F and G) and MMP and ATP levels are significantly increased (Fig. 2K and L, fig. S7H), hinting that microglia are activated by enantiomeric gels. IF staining showed that D-gel downregulated the pro-inflammatory subtype marker inducible nitric oxide synthase (iNOS) and upregulated the pro-regenerative subtype marker arginase (Arg, Fig. 2M). Flow cytometry revealed that the pro-inflammatory subtype accounted for 6.98% in the D-gel group, 0.16-fold lower than in the L-gel group, and the pro-regenerative subtype accounted for 29.04%, 1.74-fold higher than in the L-gel group (Fig. 2N, fig. S8). These in vitro results suggest that intracellular tension relaxation inhibits pro-inflammatory polarization and promotes pro-regenerative polarization in microglia.

To evaluate in vivo responses, enantiomeric hydrogels were injected into severe rat SCI models and gelled in situ at the lesion core. IF staining of the lesion core at acute phase (postoperative day 2) and subacute phase (day 7) further corroborated the intracellular tension relaxation induced pro-inflammatory polarization inhibition and pro-regenerative polarization promotion in microglia, compared to the L-gel and saline groups (Fig. 2O). The immune cytokine levels of spinal cord lesion were analyzed using high-throughput protein microarray technology (Fig. 2P). With D-gel injection, the pro-inflammatory cytokines were massively downregulated during both acute phase and subacute phase. Meanwhile, pro-regenerative cytokines were generally upregulated during the subacute phase, with no significant differences observed in the acute phase, which aligns with the inflammation timeline, where regenerative responses occur later. Collectively, these results demonstrate that D-gel-induced intracellular tension relaxation suppresses post-injury inflammation and promotes pro-regenerative polarization along with the corresponding cytokine secretion, preventing secondary inflammation damage following SCI.

SCI repair under enantiomer-engineered ECM mechanotransduction

The long-term rehabilitation of severe SCI after enantiomeric hydrogel injection (28 days) was investigated subsequently. In the D-gel group, Basso-Beattie-Bresnahan (BBB) scores, as well as movement velocity and activity time in the open field (Fig. 3A to D) were significantly increased, compared to the L-gel and saline groups. Meanwhile, the withdrawal latency response to thermal stimulus (Fig. 3E) was significantly reduced. The footprints exhibited restored movement with spread toes and sustained coordination of forelimbs and hindlimbs (Fig. 3F, fig. S9B). Additionally, the electrophysiological transduction (Fig. 3G) was successfully reconstructed with enhanced amplitude and diminished latency in the D-gel group (Fig. 3H and I), while no signals were observed in the saline group. These results demonstrate that D-gel-mediated intracellular tension relaxation facilitates locomotor recovery and accelerates sensory feedback after SCI.

Biotinylated dextran amine (BDA) was administered to anterogradely tract the axon regrowth. In rat injected with saline or L-gel, clear cavitation, resulting from secondary inflammation damage, and few regrown axons was observed within the lesion, whereas we observed substantial tissue and some regrown axons across the lesion core in the D-gel group (Fig. 3J, fig. S10A and B). The tissue in the lesion core was primarily constituted of neurons with a lack of astrocytes (fig. S10C). And no apparent astrocyte scars formed around the lesion in the D-gel group, compared to the dense population of reactive astrocytes at the lesion borders in the L-gel and saline groups, which strongly inhibits axonal regeneration *(49)*. Both cholinergic neurons (CHAT) and serotonergic neurons (5HT), locomotor function-related neurons, in the lesion were also observed improved in the D-gel group (Fig. 3K, fig. S11). The demyelination of white matter in distal lesion was determined according to myelin basic protein (MBP, Fig. 3L, fig. S12). MBP exhibited alignment and wrapping around axons in the D-gel group, whereas disordered and scattered in the L-gel and saline groups, revealing effective anti-demyelination after D-gel injection. Additionally, ECM component laminin was significantly increased and distributed around nerves in the spinal cord (Fig. 3M and N, fig. S13), indicating neuron supporting of the reconstructed ECM. Our observations suggested that D-gel treatment enabling intracellular tension relaxation significantly enhances spinal cord recovery, inhibiting glial scar formation and demyelination.

Single-nucleus transcriptome atlas following SCI

To obtain a deeper insight into the single-cell characteristics following SCI under the enantiomer-engineered ECM mechanical stimulus, we performed single-nucleus RNA-sequence (snRNA-seq) on spinal cords collected at day 10 post-injury. Coarse clustering identified 10 cell types (fig. S14), among which astrocytes, microglia, and neurons were further refined with hierarchical clustering due to their dramatic changes after injury *(49)*. We identified 8 astrocyte clusters using unbiased clustering (Fig. 4A) and analyzed their gene characteristics through KEGG pathway enrichment. Cluster 1-3 were diverse reactive astrocytes as we discussed in Supplementary Text (fig. S15) and showed little fluctuation in numbers across three groups. Cluster 6-8 were excluded here due to their minimal cell numbers and lack of significant changes. In cluster 4, substantially upregulated neurodegenerative disease-related pathways and marker genes indicated pathological degeneration and metabolic dysfunction (Fig. 4B and C). Gene set variation analysis (GSVA) across three groups (Fig. 4D) showed downregulation of all neurodegenerative pathways in the D-gel group, which, along with the greatly reduced cluster 4 percentage (Fig. 4A), suggested that intracellular tension relaxation protected astrocytes from degeneration after SCI. In cluster 5, top upregulated morphogenesis-related pathways (Fig. 4E) strongly indicated their neurogenesis function, along with specific marker genes involved in neurodevelopment, growth factors, transcriptional factors, ECM components, and ECM proteases (Fig. 4F, fig. S16). This gene expression characteristics of cluster 5 highly matches the astrocyte gene expression profile observed in vitro culture on D-gel through RNA-seq (Fig. 2H to J), both showing strong ECM remolding and neurogenesis activity. The percentage of cluster 5 in the D-gel group increased dramatically, reaching 4.43-fold of the L-gel group. Meanwhile, these morphogenesis-related pathways and genes were significantly upregulated in the D-gel group (Fig. 4G and H). These results provide single-cell evidence that intracellular tension relaxation effectively activates ECM remodeling and neurogenic activity in astrocytes following SCI.

Microglia were clustered as M0-activated, M1-proinflamatory, M2-proregenerative, and M3-others, based on reported marker genes *(50)* (Fig. 4I, fig. S17). M0 cells were most abundant, slightly decreased in the D-gel group. M1 showed minimal differences, while M2 significantly

increased in the D-gel group, 1.9 times higher than L-gel. Meanwhile, the pro-inflammatory genes were generally downregulated and the pro-regenerative genes were massively upregulated in the D-gel group (Fig. 4J). These results further validated the anti-inflammatory and pro-regenerative responses of microglia to D-gel-mediated intracellular tension relaxation, confirming to the in vitro and in vivo results. Neurons were clustered as glutamatergic neuron (Glu-N), GABAergic neuron (GABA-N), cholinergic motor neuron (Chol-N), dopaminergic neuron (DA-N), and serotonergic neuron (5HT-N), according to their transmitters (Fig. 4K) *(51)*.We classified specific KEGG pathways in each cluster and compared their gene set levels across three groups and corresponding clusters through GSVA (Fig. 4L to N, fig. S18), revealing that D-gel injection upregulated pathways and genes involved in synapse, cellular metabolism and homeostasis, and massively downregulated pathways and genes involved in degenerative diseases, cell death and oxidative stress. These results further corroborate that intracellular tension relaxation induced by D-gel provides neuroprotection and mitigates degeneration after SCI.

Single-nucleus transcriptome atlas: cellular communication

To determine how these cells interact, we performed CellChat to analyze the cellular communication patterns among these neurons, astrocyte cluster 5 (AstC5), M1 and M2 microglia. The overall interaction intensity network of the ligand-receptors (Fig. 5A) highlighted the strongest interactions between neurons, with AstC5 and M1 and M2 microglia influencing neurons. Enantiomeric hydrogel-treatment groups exhibited comprehensive communication, which is higher in the D-gel group, whereas the saline group showed minimal interaction, with GABA-N, 5HT-N, and DA-N remaining isolated. The heatmap of significant ligand-receptor pairs (fig. S19 to 21) and the corresponding outgoing/incoming signaling patterns (Fig. 5B, fig. S22) reveal the signaling pathways where one cell type provides ligands and another provides receptors. Neurons interacted with each other through neurotransmitter/synapse (Glutamate, NRXN, ADGRL, GABA-B) and intercellular adhesion/signaling (PTPR, NEGR, NCAM). Further comparing the intensity of these pathways across all three groups (Fig. 5C, fig. S23A) revealed that the D-gel group exhibited more ligand-cell to receptor cell pairs and stronger interaction intensities, represented by a greater number and thicker interaction lines in the figure, indicating enhanced synaptic signaling and inter-neuronal communication. This result was consistent with the previous observation that D-gel facilitated functional recovery and electrophysiological reconstruction and upregulated synapse-related genes (Fig.3A to I, 4M).

AstC5 exerted its effect on neurons and microglia through Laminin and Collagen pathways (Fig. 5D, fig. S23B), with enhanced intensities in the D-gel group, where AstC5 served as the primary ligand provider and other cells provided the corresponding receptors. As described above, ECM components, particularly laminin, were significantly upregulated by D-gel both in vitro and in vivo (Fig. 2I, 3M and N). These findings collectively validate that ECM remolding induced by D-gel-mediated intracellular tension relaxation promotes nerve repair comprehensively. Additionally, AstC5 influenced neurons exclusively through PTN, Netrin, WNT, and BMP pathways (Fig.5E, fig. S23C), where PTN and BMP are growth factors, Netrin is neural navigation cue, and WNT is a key developmental signaling pathway, all of which are crucial for neurogenesis. Their improvement in the D-gel group indicated that D-gel-upregulated factors related to growth and development (Fig. 2J, 4H, fig. S18A) successfully communicated with neurons, demonstrating intracellular tension relaxation-maneuvered neurogenesis on a deeper level.

APP (amyloid precursor protein) pathway, closely associated with the pathogenesis of neurodegeneration diseases, was the primary pathway through which other cells affected

microglia (Fig. 5F), indicating that the degeneration of astrocytes and neurons activates microglia, particularly inflammation (M1-microglia), which is decreased in the D-gel group compared to L-gel. Additionally, as we described above, D-gel downregulates the neurodegeneration disease-related genes and prevents astrocytes and neurons from degeneration (Fig. 4D and N). These findings collectively demonstrated that the D-gel further mitigates inflammation damage through neuroprotection and anti-degeneration, in addition to direct pro-inflammatory polarization inhibition and pro-regenerative polarization improvement.

Overall, in vivo experiments demonstrated that D-gel-mediated intracellular tension relaxation maneuvered ECM remolding and neurogenesis in astrocytes and facilitated synaptic signaling communication of neurons. The neurodegeneration after SCI was also inhibited, which mitigated inflammation response. Meanwhile, pro-inflammatory polarization and gene expression of microglia was suppressed and pro-regenerative polarization and gene expression was enhanced directly. These intracellular tension relaxation-driven effects collectively promote spinal cord repair post-injury.

Neurogenic morphology changes maneuver neurogenesis through epigenetic remolding and mechanosensitive ion channel

However, it is generally accepted that mechanical morphogenesis is driven by strong adhesion-induced high intracellular tension *(52, 53)*, particularly in studies focusing on how L-chiral ECM with high adhesion promotes non-neural cell proliferation *(23, 25, 54)*, and that the cytoskeletal contractility transfers this tension to the nucleus and cell membrane, activating mechanosensitive pathways *(55, 56)*. The neurogenesis activation by intracellular tension relaxation appears to be exceptional, highlighting a distinct response of neural cells to mechanical signals. Considering the remarkable morphology transformation with disoriented spreading and retracted protrusion on D-gel, we hypothesized that the key factor was the variation of neurogenic morphology.

We reconstructed 3D models of the cell membrane and corresponding nucleus of astrocytes (Fig. 6A) to quantify their volumes. Statistical analyses (Fig. 6B) revealed a positive correlation between cell volume and nuclear volume and that both cell and nuclear volumes in the D-gel group significantly increased, reaching 1.74-fold and 2.29-fold of the L-gel group, respectively. These results indicated osmotic swelling of neural cells and their nuclei after intracellular tension relaxation, which could change cell membrane tension and nucleic stiffness *(57)*. We then used a live cell fluorescent probe (Flipper-TR®) combined with fluorescence lifetime imaging microscopy (FLIM) to assess the cell membrane tension (fig. S24A). The significantly prolonged fluorescence lifetime on D-gel demonstrated the increased membrane tension (Fig. 6C and D), which typically leads to membrane rigidity enhancement and fluidity reduction. This was validated by significantly increased fluorescent half-recovery time after photobleaching (FRAP) on the cell membrane, (Fig. 6E and F, fig. S24B), further confirming the elevated cell membrane tension, which can pull open mechanosensitive ion channels *(58, 59)*. IF staining and Western blot (WB) assays revealed the significant clustering and upregulated expression of Piezo 1 and transient receptor potential cation channel subfamily V member 4 (TRPV4, Fig. 6G and H), suggesting cooperatively enhanced ion channel efficiency and opening *(58)*. The resulted Ca^{2+} influx (Fig. 6I and fig. S25) was subsequently demonstrated improved, which can initiate morphogenesis through multiple Ca^{2+}-dependent cascades *(60, 61)*. In the nucleus, the nuclear intermediate filament Lamin A/C, which carries nuclear tension and transfers it into chromatin condensation *(62)* exhibited significant upregulation in the D-gel group (Fig. 6J and M), corroborating the improved nuclear stiffness and suggesting chromatin unfolding. The reduced histone deacetylase (HDAC, an enzyme catalyzing chromatin folding *(63)*) demonstrated the chromatin unfolding and enhanced transcriptional accessibility. The improved nuclear

translocation of Yes-associated protein (YAP, a mechanosensitive transcriptional activator *(64)*, Fig. 6K to M) validated transcriptional activation, aligning with the substantial transcriptome variation (Fig. 2J).

Discussion

Our work demonstrates that intracellular tension relaxation induced by ECM mechanics activates neurogenesis in astrocytes and modulates immune responses of microglia, leading to neuroprotection, synapse signaling enhancement, and inflammatory damage inhibition, consequently facilitating functional recovery from SCI. The neurogenesis activation in astrocytes aligns with our previous study *(29)*, where D-enantiomeric hydrogel enhances morphogenetic processes in multiple neural cells, including immortalized neuron, neuron-like cell, and Schwann cell, further validating that intracellular tension relaxation maneuvers neurogenesis, despite not observing this phenomenon directly in spinal cord neurons due to their advanced differentiation.

However, numerous studies have shown that non-neural cells typically exhibit inhibited morphogenesis, particularly in proliferation, when cultured on D-enantiomeric matrices *(23-27, 52-54)*. These findings imply that intracellular tension relaxation-induced morphogenesis may be characteristic for neural cells, which is further highlighted by the mechanism that the consequent change of neurogenic morphology activates the downstream mechanical signaling. During neural cell maturation, as protrusions are specialized to elongate for signal transmission, neurons lose their regenerative capacity *(3)*. The morphological changes induced by intracellular tension relaxation may reverse this process. This suggests that the distinctive response to mechanical signals may play a crucial role in neurodevelopment. Mechanical force can directly modulate the developmental state of neural cells, encouraging a neuro-specific signal for in vitro neural organoids and therapies for neural injury repair.

Meanwhile, we revealed the anti-inflammation and pro-regeneration in microglia responding to intracellular tension relaxation, although we did not explore the detailed mechanotransduction, which have been reported extensively, including YAP nuclear translocation and mechanosensitive ion channels *(65, 66)*. These findings about neuro-specialized immune cell provide wider insights within the central nervous system into the role of mechanical signals in regulating immune responses, and offer additional approaches for mitigating secondary inflammatory damage following SCI.

References and Notes

1. S. A. Kent, V. E. Miron, Microglia regulation of central nervous system myelin health and regeneration. *Nature Reviews Immunology* **24**, 49-63 (2024).
2. T. H. Hutson, S. Di Giovanni, The translational landscape in spinal cord injury: focus on neuroplasticity and regeneration. *Nature Reviews Neurology* **15**, 732-745 (2019).
3. B. J. Hilton, J. M. Griffin, J. W. Fawcett, F. Bradke, Neuronal maturation and axon regeneration: unfixing circuitry to enable repair. *Nature Reviews Neuroscience* **25**, 649-667 (2024).
4. M. A. Anderson *et al.*, Required growth facilitators propel axon regeneration across complete spinal cord injury. *Nature* **561**, 396-400 (2018).
5. H. Kumamaru *et al.*, Generation and post-injury integration of human spinal cord neural stem cells. *Nature Methods* **15**, 723-731 (2018).
6. E. Llorens-Bobadilla *et al.*, A latent lineage potential in resident neural stem cells enables spinal cord repair. **370**, eabb8795 (2020).
7. J. W. Squair *et al.*, Recovery of walking after paralysis by regenerating characterized neurons to their natural target region. **381**, 1338-1345 (2023).
8. Z. Álvarez *et al.*, Bioactive scaffolds with enhanced supramolecular motion promote recovery from spinal cord injury. **374**, 848-856 (2021).
9. H. De Belly, E. K. Paluch, K. J. Chalut, Interplay between mechanics and signalling in regulating cell fate. *Nature*

Reviews Molecular Cell Biology **23**, 465-480 (2022).
10. M. Valet, E. D. Siggia, A. H. Brivanlou, Mechanical regulation of early vertebrate embryogenesis. *Nature Reviews Molecular Cell Biology* **23**, 169-184 (2022).
11. S. Quintes *et al.*, Zeb2 is essential for Schwann cell differentiation, myelination and nerve repair. *Nature Neuroscience* **19**, 1050-1059 (2016).
12. H. Sabelström *et al.*, Resident Neural Stem Cells Restrict Tissue Damage and Neuronal Loss After Spinal Cord Injury in Mice. **342**, 637-640 (2013).
13. S. Chen *et al.*, Macrophages in immunoregulation and therapeutics. *Signal Transduction and Targeted Therapy* **8**, 207 (2023).
14. V. S. Meli *et al.*, YAP-mediated mechanotransduction tunes the macrophage inflammatory response. **6**, eabb8471 (2020).
15. E. Moeendarbary *et al.*, The soft mechanical signature of glial scars in the central nervous system. *Nature Communications* **8**, 14787 (2017).
16. E. Kuhl, Mechanical Cues in Spinal Cord Injury. *Biophys J* **115**, 751-753 (2018).
17. H. Hong *et al.*, Dynamic Ligand Screening by Magnetic Nanoassembly Modulates Stem Cell Differentiation. *Advanced Materials* **34**, 2105460 (2022).
18. T. Kamperman *et al.*, Tethering Cells via Enzymatic Oxidative Crosslinking Enables Mechanotransduction in Non-Cell-Adhesive Materials. **33**, 2102660 (2021).
19. O. Chaudhuri, J. Cooper-White, P. A. Janmey, D. J. Mooney, V. B. Shenoy, Effects of extracellular matrix viscoelasticity on cellular behaviour. *Nature* **584**, 535-546 (2020).
20. L. M. Wingler, R. J. Lefkowitz, Conformational Basis of G Protein-Coupled Receptor Signaling Versatility. *Trends in Cell Biology* **30**, 736-747 (2020).
21. P. Peluso, B. Chankvetadze, Recognition in the Domain of Molecular Chirality: From Noncovalent Interactions to Separation of Enantiomers. *Chemical Reviews* **122**, 13235-13400 (2022).
22. D. R. Griffin *et al.*, Activating an adaptive immune response from a hydrogel scaffold imparts regenerative wound healing. *Nature Materials* **20**, 560-569 (2021).
23. J. Liu *et al.*, The Cooperative Effect of Both Molecular and Supramolecular Chirality on Cell Adhesion. *Angewandte Chemie International Edition* **57**, 6475-6479 (2018).
24. A. Motealleh, H. Hermes, J. Jose, N. S. Kehr, Chirality-dependent cell adhesion and enrichment in Janus nanocomposite hydrogels. *Nanomedicine: Nanotechnology, Biology and Medicine* **14**, 247-256 (2018).
25. G.-F. Liu, D. Zhang, C.-L. Feng, Control of Three-Dimensional Cell Adhesion by the Chirality of Nanofibers in Hydrogels. *Angewandte Chemie International Edition* **53**, 7789-7793 (2014).
26. F. Zhou *et al.*, Cell adhesion on chiral surface: The role of protein adsorption. *Colloids and Surfaces B: Biointerfaces* **90**, 97-101 (2012).
27. H. Lu *et al.*, Fluorine Substitution Tunes the Nanofiber Chirality of Supramolecular Hydrogels to Promote Cell Adhesion and Proliferation. *Advanced Fiber Materials* **5**, 377-387 (2023).
28. W. Deng *et al.*, Graphene oxide-doped chiral dextro-hydrogel promotes peripheral nerve repair through M2 polarization of macrophages. *Colloids and Surfaces B: Biointerfaces* **233**, 113632 (2024).
29. Y. Li *et al.*, Unique Chirality Selection in Neural Cells for D-Matrix Enabling Specific Manipulation of Cell Behaviors. *Advanced Materials* **35**, 2301435 (2023).
30. K. Sato, W. Ji, Z. Álvarez, L. C. Palmer, S. I. Stupp, Chiral Recognition of Lipid Bilayer Membranes by Supramolecular Assemblies of Peptide Amphiphiles. *ACS Biomaterials Science & Engineering* **5**, 2786-2792 (2019).
31. K. Baranes, H. Moshe, N. Alon, S. Schwartz, O. Shefi, Neuronal Growth on l- and d-Cysteine Self-Assembled Monolayers Reveals Neuronal Chiral Sensitivity. *ACS Chemical Neuroscience* **5**, 370-376 (2014).
32. N. Sun *et al.*, Bio-inspired chiral self-assemblies promoted neuronal differentiation of retinal progenitor cells through activation of metabolic pathway. *Bioactive Materials* **6**, 990-997 (2021).
33. Y. He *et al.*, Biomimetic Chiral Nanotopography for Manipulating Immunological Response. *Advanced Functional Materials* **34**, 2313157 (2024).
34. S. Jiang *et al.*, Chirality Bias Tissue Homeostasis by Manipulating Immunological Response. *Advanced Materials* **34**, 2105136 (2022).
35. L. Xu *et al.*, Enantiomer-dependent immunological response to chiral nanoparticles. *Nature* **601**, 366-373 (2022).
36. W. Ahmed, M. Karabaliev, C. Gao, Taking chiral polymers toward immune regulation. *Journal of Polymer Science* **60**, 2213-2224 (2022).
37. R. M. Ransohoff, A polarizing question: do M1 and M2 microglia exist? *Nature Neuroscience* **19**, 987-991 (2016).
38. N. Yamaguchi, H. Knaut, Focal adhesion-mediated cell anchoring and migration: from in vitro to in vivo. *Development* **149**, dev200647 (2022).

39. S. Schumacher *et al.*, Structural insights into integrin α₅β₁ opening by fibronectin ligand. **7**, eabe9716 (2021).
40. T. Arimori *et al.*, Structural mechanism of laminin recognition by integrin. *Nature Communications* **12**, 4012 (2021).
41. A. J. Stone, Natural Bond Orbitals and the Nature of the Hydrogen Bond. *The Journal of Physical Chemistry A* **121**, 1531-1534 (2017).
42. K. Legerstee, B. Geverts, J. A. Slotman, A. B. Houtsmuller, Dynamics and distribution of paxillin, vinculin, zyxin and VASP depend on focal adhesion location and orientation. *Scientific Reports* **9**, 10460 (2019).
43. K. R. Long, W. B. Huttner, How the extracellular matrix shapes neural development. *Open Biology* **9**, 180216 (2019).
44. A. u. R. Aziz *et al.*, The explorations of dynamic interactions of paxillin at the focal adhesions. *Biochimica et Biophysica Acta (BBA) - Proteins and Proteomics* **1870**, 140825 (2022).
45. C. Ciobanasu, B. Faivre, C. Le Clainche, Actomyosin-dependent formation of the mechanosensitive talin–vinculin complex reinforces actin anchoring. *Nature Communications* **5**, 3095 (2014).
46. A. Zemel, Active mechanical coupling between the nucleus, cytoskeleton and the extracellular matrix, and the implications for perinuclear actomyosin organization. *Soft Matter* **11**, 2353-2363 (2015).
47. D. E. Rassier, A. Månsson, Mechanisms of myosin II force generation: insights from novel experimental techniques and approaches. *Physiological Reviews* **105**, 1-93 (2024).
48. J. Guo, Y. Wang, F. Sachs, F. Meng, Actin stress in cell reprogramming. *Proceedings of the National Academy of Sciences of the United States of America* **111**, E5252-5261 (2014).
49. M. A. Skinnider *et al.*, Single-cell and spatial atlases of spinal cord injury in the Tabulae Paralytica. *Nature* **631**, 150-163 (2024).
50. T. R. Hammond *et al.*, Single-Cell RNA Sequencing of Microglia throughout the Mouse Lifespan and in the Injured Brain Reveals Complex Cell-State Changes. *Immunity* **50**, 253-271.e256 (2019).
51. K. Morarach *et al.*, Diversification of molecularly defined myenteric neuron classes revealed by single-cell RNA sequencing. *Nature Neuroscience* **24**, 34-46 (2021).
52. H. Zhang *et al.*, A tension-induced mechanotransduction pathway promotes epithelial morphogenesis. *Nature* **471**, 99-103 (2011).
53. M. A. Wozniak, C. S. Chen, Mechanotransduction in development: a growing role for contractility. *Nature Reviews Molecular Cell Biology* **10**, 34-43 (2009).
54. S. Zhang *et al.*, l-cysteine-modified chiral gold nanoparticles promote periodontal tissue regeneration. *Bioactive Materials* **6**, 3288-3299 (2021).
55. F. Yang *et al.*, The effect of incorporating RGD adhesive peptide in polyethylene glycol diacrylate hydrogel on osteogenesis of bone marrow stromal cells. *Biomaterials* **26**, 5991-5998 (2005).
56. B. D. Cosgrove *et al.*, N-cadherin adhesive interactions modulate matrix mechanosensing and fate commitment of mesenchymal stem cells. *Nature Materials* **15**, 1297-1306 (2016).
57. B. Enyedi, M. Jelcic, P. Niethammer, The Cell Nucleus Serves as a Mechanotransducer of Tissue Damage-Induced Inflammation. *Cell* **165**, 1160-1170 (2016).
58. B. Xiao, Mechanisms of mechanotransduction and physiological roles of PIEZO channels. *Nature Reviews Molecular Cell Biology* **25**, 886-903 (2024).
59. K. D. Nadezhdin *et al.*, Structure of human TRPV4 in complex with GTPase RhoA. *Nature Communications* **14**, 3733 (2023).
60. M. L. Delco, L. J. Bonassar, Targeting calcium-related mechanotransduction in early OA. *Nature Reviews Rheumatology* **17**, 445-446 (2021).
61. S. Luan, C. Wang, Calcium Signaling Mechanisms Across Kingdoms. **37**, 311-340 (2021).
62. C. Uhler, G. V. Shivashankar, Regulation of genome organization and gene expression by nuclear mechanotransduction. *Nature Reviews Molecular Cell Biology* **18**, 717-727 (2017).
63. T. Sato *et al.*, A FAK/HDAC5 signaling axis controls osteocyte mechanotransduction. *Nature Communications* **11**, 3282 (2020).
64. S. Dupont *et al.*, Role of YAP/TAZ in mechanotransduction. *Nature* **474**, 179-183 (2011).
65. H. Du *et al.*, Tuning immunity through tissue mechanotransduction. *Nature Reviews Immunology* **23**, 174-188 (2023).
66. V. S. Meli *et al.*, YAP-mediated mechanotransduction tunes the macrophage inflammatory response. *Science Advances* **6**, eabb8471.

Acknowledgments: †These authors contributed equally to this work. The authors thank Dr. Siying Qin in the Core Facilities (School of Life Sciences, Peking University), for assistance with FluidFM BOT. The authors would like to thank Jiao Lu and Guolong Meng (College of Biomedical Engineering, Sichuan University) for their assistance with laser confocal microscopy. We would like to thank Linzhu Li in the Life Science Core Facilities (College of Life Sciences, Sichuan University) for help of digital scanning system and laser confocal microscopy. We thank Wenwu Wang (College of Materials Science & Engineering, Sichuan University) for his help of AFM capturing and analysis. We also thank Prof. Jiang Wu and Dr. Jirui Wen for their support on flow cytometry. We thank ChatGPT (OpenAI) for providing language editing support and improving the grammatical accuracy of this paper.

Funding: This work was funded by the National Key R&D Program of China (2023YFC2410403).

Author contributions:

Conceptualization: YL, QA

Methodology: YW, XF, YL, HZ, RL, XL, XL

Visualization: YW, YL, RC, ZY

Supervision: QA, ZH, GY

Writing – original draft: YL, YW

Writing – review & editing: YL, QA, YW

Competing interests: The authors declare no competing interest.

Data and materials availability: All data needed to evaluate the conclusions in the paper are present either in the main text or the supplementary materials

Supplementary Materials

Materials and Methods

Supplementary Text

Figs. S1 to S25

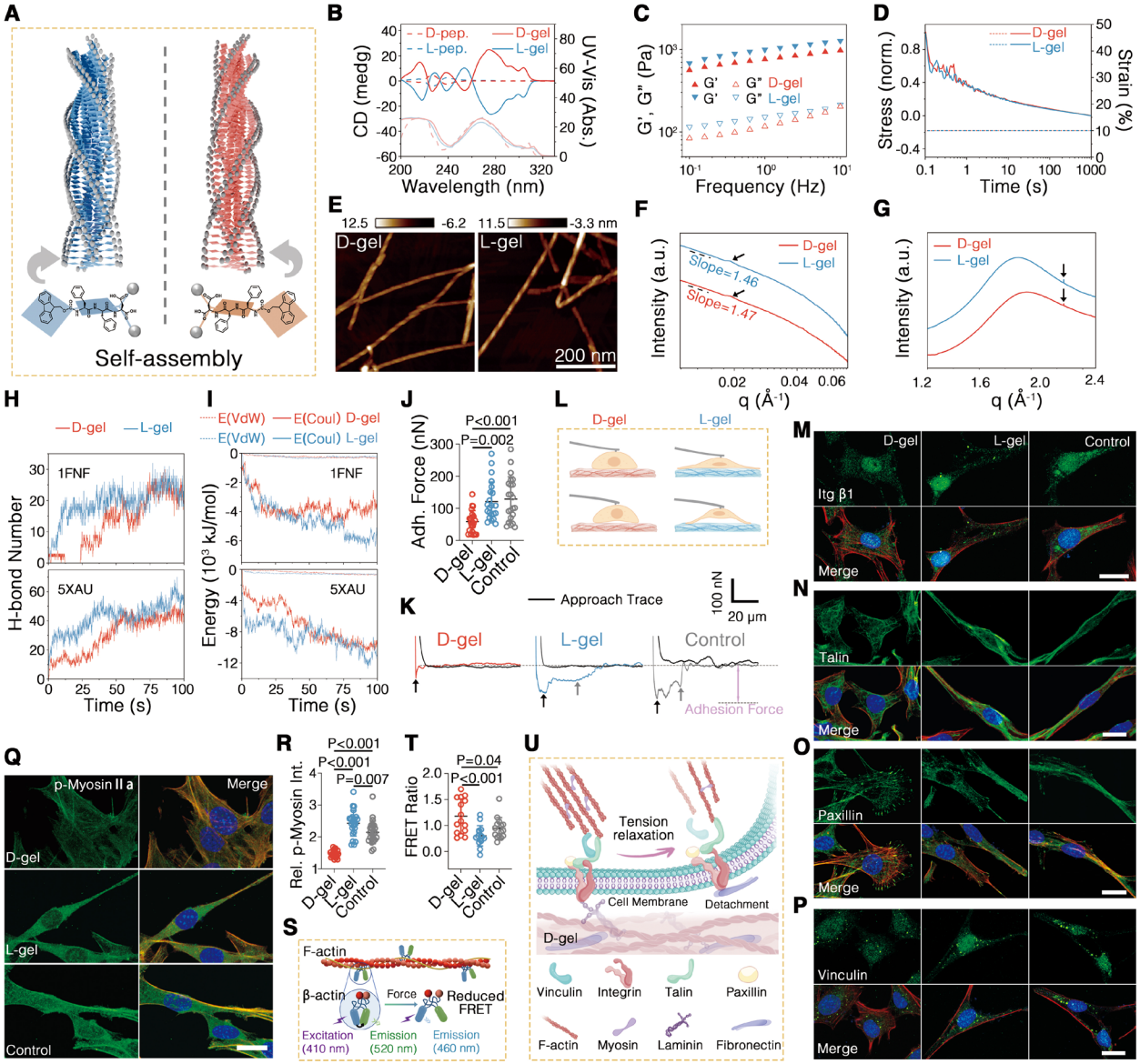

Fig. 1. Engineered enantiomeric hydrogels manipulating intracellular tension. (A) Schematic representation of Fmoc-FFD enantiomers self-assembly into nanofiber hydrogels with mirror-symmetric helices. (B) CD spectra (in dark colors) and corresponding UV-vis spectra (in light colors) of Fmoc-FFD peptide enantiomers and corresponding hydrogels. (C, D) Rheological spectra of enantiomeric hydrogels presenting frequency-dependent strength (C) and stress relaxation (D). (E) AFM micrographs of enantiomeric hydrogels. (F, G) SAXS patterns (F) and WAXS patterns (G) of enantiomeric hydrogels. The scattering intensities were offset vertically for clarity; the characteristic peaks were indicated by black arrows. (H, I) Hydrogen bond formation (H) and interaction energy (I) between enantiomeric assemblies and fibronectin (1FNF) or laminin fragment (5XAU) from MD simulations. (J, K, L) Adhesion force magnitude (J) and force-probe displacement curves (K) between astrocytes and culture matrix measured by SCFS, with a schematic representation (L) of the experimental setup on enantiomeric hydrogels. (M, N, O, P, Q, R) Representative IF staining micrographs of astrocytes cultured on enantiomeric hydrogels, with marker in green, cytoskeleton in red, and nucleus in blue. Scale bar = 20 μm. Fluorescence intensity of p-Myosin was quantified in individual cells (R). (**S, T**)

Schematic representation illustrating the process that cytoskeleton force reduces FRET efficiency (S), and FRET efficiency of astrocytes cultured on enantiomeric hydrogels (T). (U) Schematic representation illustrating D-gel-induced intracellular tension relaxation.

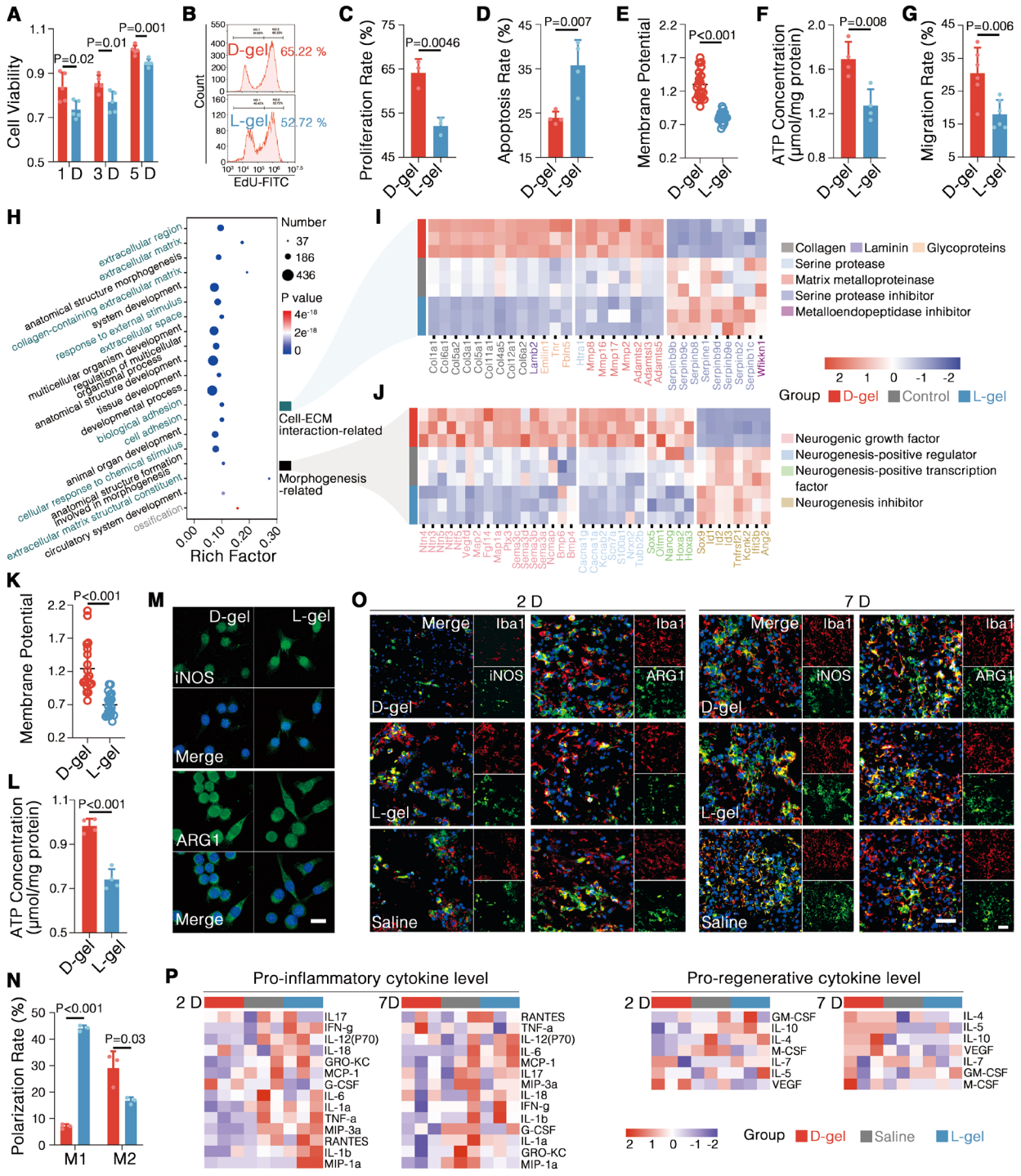

Fig. 2. Morphogenesis in astrocytes and immunomodulation in microglia maneuvered by intracellular tension relaxation. (A-G) Morphogenesis process of astrocytes cultured on enantiomeric hydrogels: cellular viability (A), flow cytometry histogram of proliferating cells (B), proliferation rate (C), apoptosis rate (D), mitochondrial membrane potential (E), ATP concentration (F), and migration rate in 24 h (G). (H, I, J) Top 20 KEGG pathways enriched in

astrocyte genes with differential expression between D-gel and L-gel groups from RNA-seq (H), and corresponding heatmaps for Cell-ECM interaction-related (I) and morphogenesis-related (J) gene expression. (K, L) Mitochondrial membrane potential (K) and ATP concentration (J) of microglia cultured on enantiomeric hydrogels. (M) Representative IF staining micrographics of microglia. iNOS labels M1 pro-inflammatory polarization, Arg1 marks M2 pro-regenerative polarization. DAPI-stained nucleus is in blue. Scale bar = 20 μm. (N) Polarization rate of microglia cultured on enantiomeric hydrogels based on flow cytometry assay. (O) Representative IF staining micrographics of spinal cord lesion on day 2 and 7 postoperatively, Iba1 labels microglia and DAPI-stained nucleus is in blue. Scale bar = 50 μm. (P, Q) Heatmaps of pro-inflammatory (P) and pro-regenerative (Q) immune cytokine levels in spinal cord lesion at day 2 and 7 postoperatively.

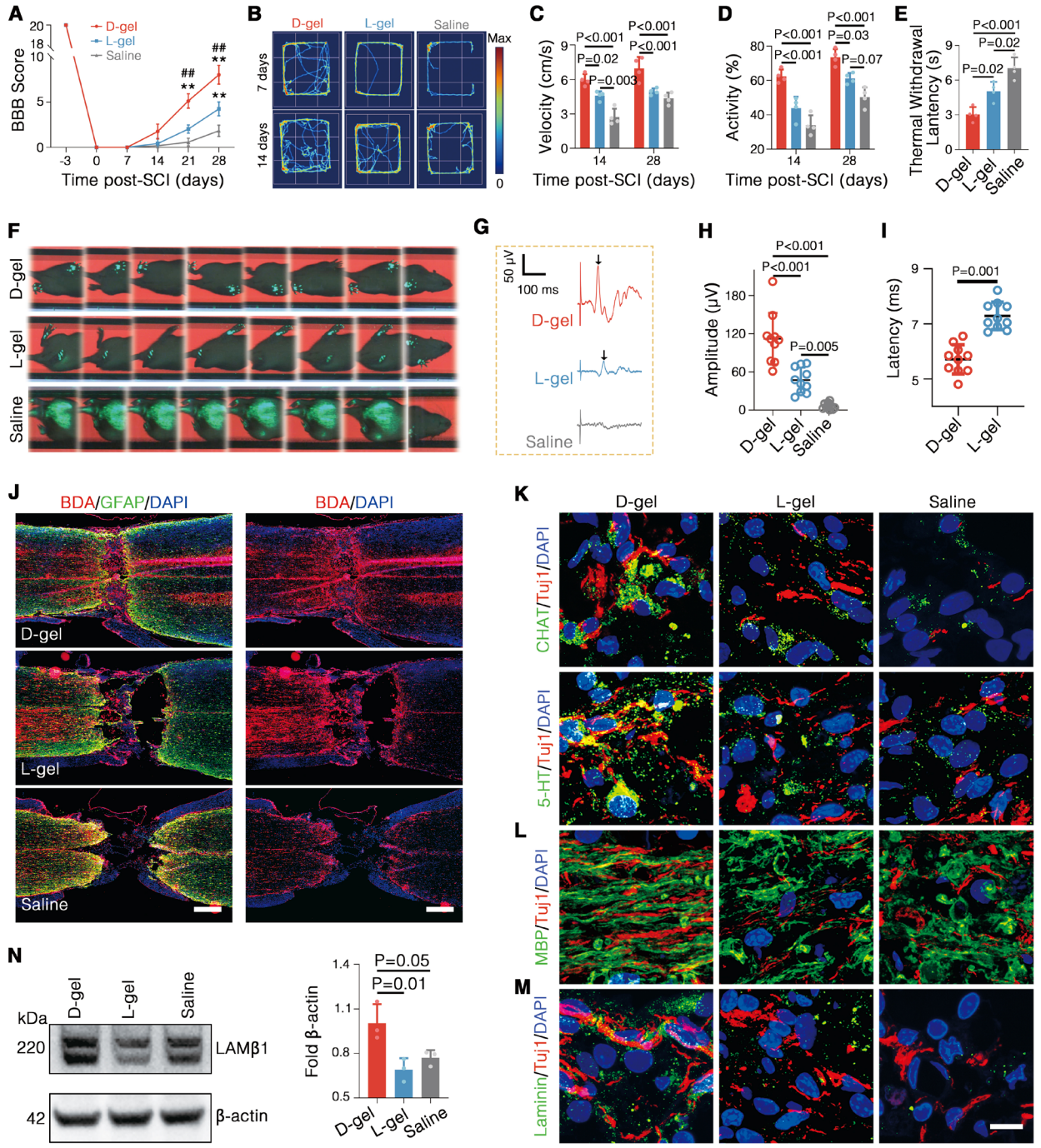

Fig. 3. SCI repair under enantiomer-manipulated mechanotransduction cues. (A-D) Locomotion recovery after SCI: BBB scores (A), activity track heatmap (B) and statistical analyses of movement velocity (C) and activity time percentage (D) in the open field. (E) Withdrawal latency response to thermal stimulus at day 28. (F) Representative motion trajectories of rat models at day 28. (G-I) Motor evoked potentials (G) and statistical analyses of amplitude (H) and latency (I) at day 28. (J) Fluorescent micrographics of longitudinal spinal cord sections. GFAP indicates astrocytes (green), BDA indicates labeled axons (red), and DAPI

indicates nuclei (blue). Scar bar = 500 μm. (K, L, M) Representative IF staining micrographics of spinal cord. Tuj1 labels neuron and DAPI labels nuclei. Scar bar = 10 μm. (N) WB results and statistics of laminin in injured spinal cord.

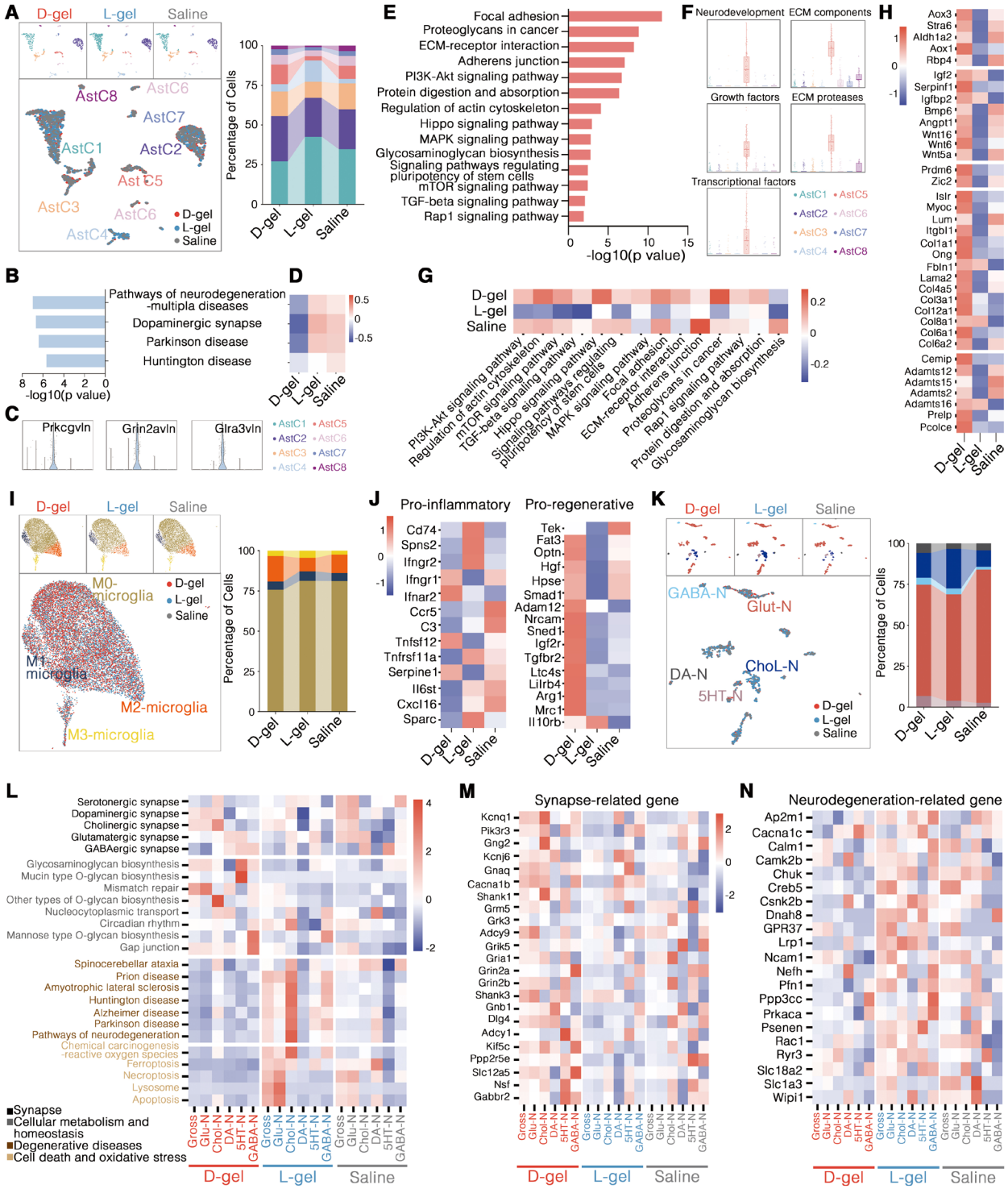

Fig. 4. The snRNA-seq atlas of spinal cord at day 10 post-injury. (A) UMAP visualizations and proportions of astrocyte clusters. (B, C, D) Degeneration-related KEGG pathways (B) top enriched in AstC4, corresponding marker gene levels across different astrocyte clusters (C), and corresponding GSVA heatmap depicting the KEGG pathway levels in AstC4 across different groups (D). (E, F, G, H) Neurogenesis-related KEGG pathways (E) top enriched in AstC5,

corresponding GSVA of marker genes classified according to gene function across different astrocyte clusters (F), and corresponding GSVA heatmap (G) depicting the KEGG pathway levels in AstC5 across different groups. Panel (H) is corresponding morphogenesis-related gene level heatmap across different groups. (I, J) UMAP visualizations and proportions of microglia clusters (I) and immune gene level heatmap across different groups (J). (K, L, M, N) UMAP visualizations and proportions of neuron clusters (K), GSVA heatmap of top enriched KEGG pathways characteristic in all neuron clusters (L), synapse-related gene level (M) and neurodegeneration-related gene level (N) heatmaps of each cluster and neuron gross across different groups.

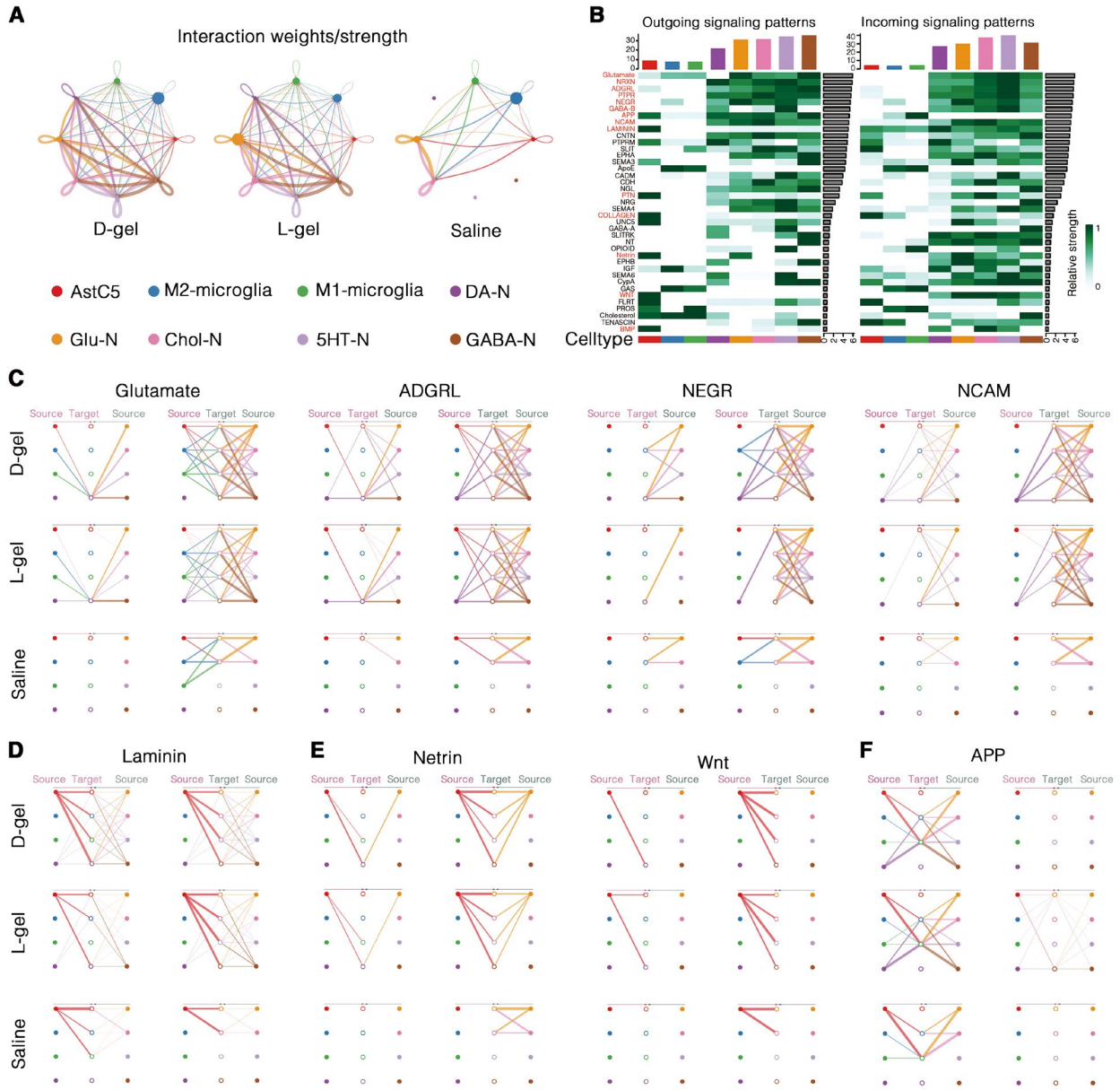

Fig. 5. Cellular communication based on snRNA-seq atlas. (A) Gross interaction strength network between AstC5, M2-microglia, M1-microglia, DA-N, Glu-N, Chol-N, 5HT-N, and GABA-N. (B) High contributed signaling pathway patterns of the D-gel group. Outgoing signaling patterns indicate ligand-providing celltypes, and incoming signaling patterns indicate receptor-providing celltypes. (C, D, E, F) Hierarchical diagram of ligand-receptor interactions within signaling pathways: pathways between neurons (C), pathways through which AstC5 affects others (D), pathways through which AstC5 influences neurons exclusively (E), pathways through which other cells impact microglia (F). Solid circles represent ligand-providing cells, hollow circles represent receptor-providing cells, and thicker lines indicate stronger signals.

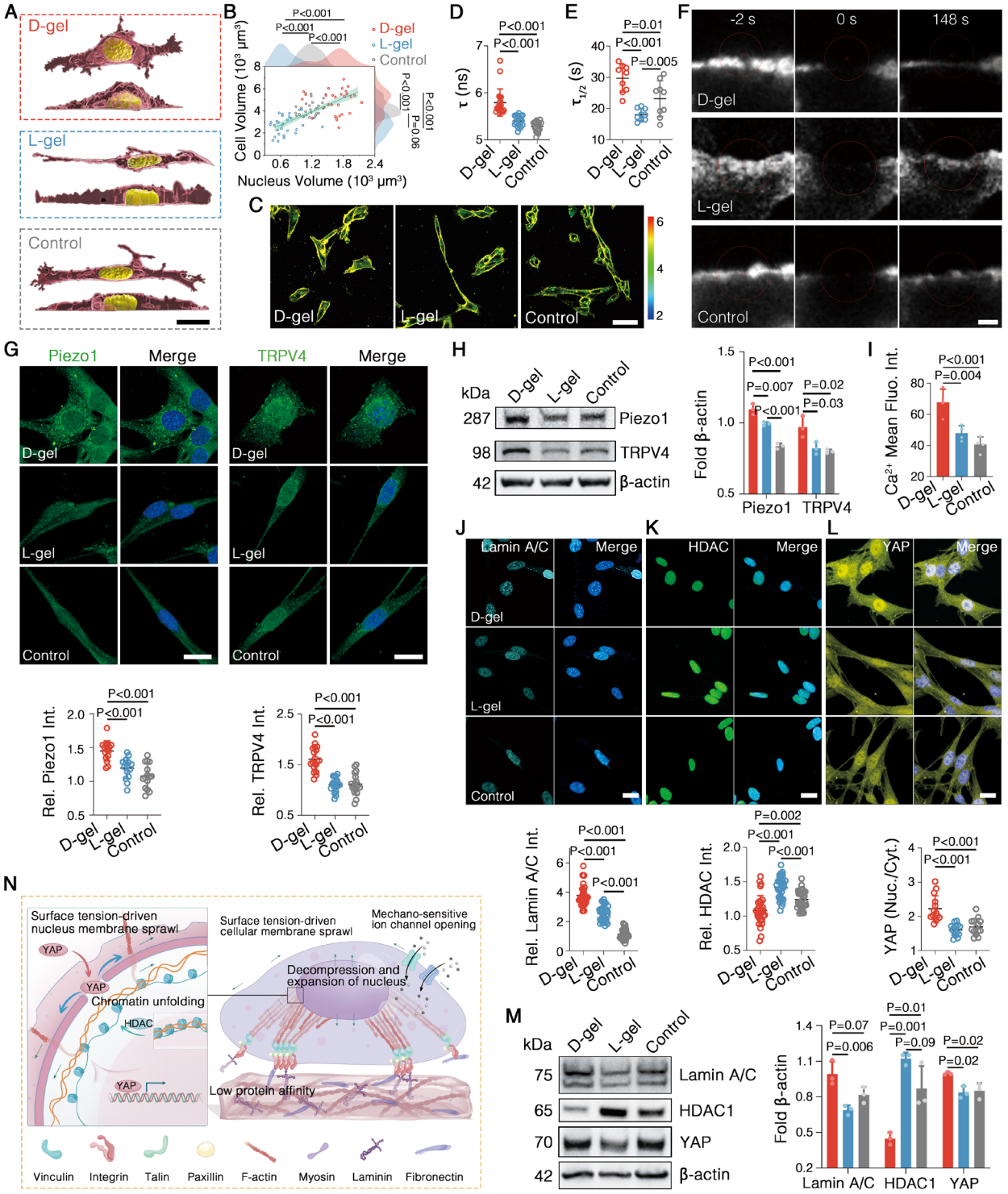

Fig. 6. Neurogenic morphology variation and downstream mechanical signaling. (A, B) Computational reconstruction of astrocyte cell nuclei and cell membranes (A) and corresponding volume statistics (B). (C, D) FLIM heatmap of astrocytes staining with Flipper-TR® (C) and corresponding fluorescence lifetime statistics (D). (E, F) Fluorescent half-recovery time after photobleaching (E) and representative micrographs (F). (G) Representative IF staining micrographs of astrocytes cultured on enantiomeric hydrogels with DAPI-stained nuclei in blue

and corresponding quantification in individual cells. (H) WB results and statistics of mechanosensitive ion channels in astrocytes. (I) Fluorescence intensity statistics of stained Ca2+ in astrocytes. (J, K, L) Representative IF staining micrographs of astrocytes for Lamin A/C (J), HDAC (K), and YAP (L) with DAPI-stained nuclei in blue and corresponding quantification in individual cells. The ratio of nuclear intensity to cytoplasmic intensity of YAP is calculated. (M) WB results and statistics of Lamin A/C, HDAC, and YAP in astrocytes. (N) Schematic representation illustrating that intracellular tension relaxation opens mechanosensitive ion channel, unfolds chromatin, and activates transcription through increasing membrane tension and nuclear stiffness. Scale bars, 30 μm (A), 50 μm (C), 2 μm (F) 20 μm (G, J, K, L).

Collectively, as illustrated in Fig. 6N, D-enantiomeric hydrogel-driven intracellular tension relaxation disrupts polarized neurogenetic morphology, leading to osmotic swelling. The expanding membrane increases both cell membrane tension and nuclear stiffness, which opens mechanosensitive ion channels, unfolds chromatin, and triggers transcription, ultimately maneuvering neurogenesis.